UNIVERSITY OF CALIFORNIA

Los Angeles

Using $Mo_{0.5}Nb_{0.5}O_2$ Solid Solutions with Varying Degrees of Phase Separation to Understand and Enhance High-Rate Electrochemical Charge Storage in a Model Lithium-Ion Battery Oxide Anode

A thesis submitted in partial satisfaction

of the requirements for the degree Master of Science

in Materials Science and Engineering

by

Ewing Yu-Wen Chen

2024

ABSTRACT OF THE THESIS

Using $Mo_{0.5}Nb_{0.5}O_2$ Solid Solutions with Varying Degrees of Phase Separation to Understand and Enhance High-Rate Electrochemical Charge Storage in a Model Lithium-Ion Battery Oxide Anode

by

Ewing Yu-Wen Chen

Master of Science in Materials Science and Engineering

University of California, Los Angeles, 2024

Professor Sarah H. Tolbert, Chair

Li-ion batteries are technologically vital for reducing reliance on fossil fuels through the electrification of transportation, particularly electric vehicles. However, many Li-ion battery materials are limited in their ability to fast-charge. Notably, first-order phase transformations during lithiation/delithiation in these materials can hinder charging speeds through slow propagation of phase fronts a limited Li-ion diffusion. In this work, we modify the tunnel-structure host material MoO_2 via cation substitution to create $Mo_{0.5}Nb_{0.5}O_2$ solid solutions with varying extents of cation mixing to induce partial phase transition suppression. We utilize operando synchrotron X-ray diffraction with electrochemical analyses to elucidate the effect of cation mixing within the solid solution on suppression of first-order insertion-induced phase transitions and their effect on electrochemical performance. We find that there are two limits to the phase

behavior. Materials synthesized a high temperature are quite crystalline, but can show clustering of Mo and Nb oxide domains in $Mo_{0.5}Nb_{0.5}O_2$, and these materials show distinct first-order phase transitions during cycling, lower capacity, poor rate performance, and decreased cycle life. The use of metal-oxide cluster precursors in the synthesis produces a similar result. In poorly crystalline $Mo_{0.5}Nb_{0.5}O_2$, the Mo and Nb remain well mixed, and the structure evolution becomes entirely single-phase/solid-solution, indicating first-order phase transition suppression. Unfortunately, the rate performance and capacity remain poor due to inhibited Li mobility in the disordered structures. Synthesizing materials at the lowest temperature that produces crystalline $Mo_{0.5}Nb_{0.5}O_2$, results in materials with partial first-order phase transition suppression, and these materials demonstrated the best capacity, rate capability, and cycle life performance. Thus, this work demonstrates cation substitution as a method to control first-order phase transition behavior in tunnel structure Li insertion host materials for battery applications.

The thesis of Ewing Yu-Wen Chen is approved.

Richard B. Kaner

Yuzhang Li

Sarah H. Tolbert, Committee Chair

University of California, Los Angeles

2024

TABLE OF CONTENTS

Introduction 1

Experimental Method 6

Synthesis of $Mo_{0.5}Nb_{0.5}O_2$ and Pure Phase NbO_2 and MoO_2 Powders 6

Structural Characterization 7

Electrochemical Testing 8

Slurry Electrode Preparation 8

Coin Cell Assembly and Electrochemistry 8

Operando Synchrotron X-ray Diffraction 9

Results and Discussion 10

Synthesis and Structural Characterization of $Mo_{0.5}Nb_{0.5}O_2$ 10

Electrochemical Characterization and Rate Performance 14

Structural Evolution Characterized via *Operando* XRD 20

Cycle-Life Performance 24

Conclusion 26

Appendix 28

References 33

LIST OF FIGURES

Figure 1: SEM and XRD Characterization 12

Figure 2: CV Curves, B-Value, ΔEP 16

Figure 3: Galvanostatic Rate Cycling Performance 19

Figure 4: Operando XRD Heat Maps and Scans 21

Figure 5: Long-Term Galvanostatic Cycling Performance 25

Figure A1: SEM Images of Loose Particles 28

Figure A2: EDS Elemental Mapping for 650 Cl 28

Figure A3: EDS Elemental Mapping for 850 Cl 28

Figure A4: EDS Elemental Mapping for 1050 Cl 29

Figure A5: EDS Elemental Mapping for 850 POM 29

Figure A6: SEM, XRD, and CV Characterization for NbO_2 30

Figure A7: SEM, XRD, and CV Characterization for MoO_2 31

Figure A8: Fitted peaks of *operando* XRD scans 32

ACKNOWLEDGEMENTS

This work was supported by the U.S. Department of Energy, Office of Basic Energy Sciences, under Award Number DE-SC0014213. *Operando* XRD experiments were conducted at beamline 11-3 of the Stanford Synchrotron Radiation Lightsource (SLAC National Accelerator Laboratory). We would like to thank Dr. Molleigh Preefer and Dr. Kevin Stone for their assistance. Use of the Stanford Synchrotron Radiation Lightsource, SLAC National Accelerator Laboratory, is supported by the U.S. Department of Energy, Office of Science, Office of Basic Energy Sciences, under Contract No. DE-AC02-76SF00515.

The present work would not have been possible without the guidance from my thesis advisor, Professor Sarah H. Tolbert, and my mentor, PhD candidate David J. Pe. I would like to express my deepest gratitude for their incredible support, expert advice, mentorship, and encouragement. I would also like to extend my thanks to every member in the Tolbert Lab for all the technical and moral support they have provided throughout my time there. Finally, I would like to sincerely thank my family and friends for their unwavering support and belief in me.

Introduction

As efforts to reduce dependence on fossil fuels increase, the significance of energy storage devices has grown commensurately. Consequently, lithium-ion battery (LIB) technologies have become widely adopted in various applications, including personal electronics and electric vehicles (EVs).[1,2] LIBs are electrochemical devices that store charge through redox reactions in which Li^+ ions are reversibly inserted into a host material. When charging a LIB, an electric current is applied to the system from an external power source, causing Li^+ ions to be extracted from the cathode and inserted into the anode. The opposite occurs during discharge: Li^+ ions are extracted from the anode and inserted into the cathode, generating an electric current.[3]

Despite continuous enhancements since their initial commercialization decades ago, LIBs are still faced with sluggish charge/discharge rates, hindering their broader adoption for EVs over internal combustion engine vehicles.[1,2,4] From a materials perspective, lithium-ion transport in the electrolyte phase (liquid or solid), charge-transfer kinetics at phase boundaries within a LIB, intrinsic electrode material electrical conductivity, and solid-state diffusion of lithium ions within the anode and cathode active material can all cause kinetic limitation,[5] but it is the solid state diffusion that is often the slowest. This occurs in part because Li^+ ion insertion and extraction in most electrode materials are often slowed due to the occurrence of first-order phase transitions.[6,7] During cycling, changes in Li-content strain the host crystal structure, driving structural rearrangement.

There are two kinds of phase transition mechanisms relevant here: continuous and discontinuous.[7] In a continuous or solid solution mechanism, the insertion host expands and contracts with the lattice parameters changing continuously as a function

of Li content.[7,8] Conversely, in a discontinuous or first-order phase transition, the nucleation and growth of a more stable phase throughout the active material must occur at a critical Li-content before additional Li can be inserted or removed. A hallmark of this type of phase transition is a miscibility gap, which corresponds to immiscible Li stoichiometries between the initial and transformed structure. This is observable as a discontinuous jump in lattice parameters from a Li-poor to Li-rich phase or vice versa.[6–8] Related to the miscibility gap is the extent of two-phase coexistence, or the voltage and capacity range in which both phases are present in the material.[9]

Discontinuous phase transitions are believed to inhibit Li insertion/extraction due to the sluggish kinetics associated with nucleating and propagating a new phase.[8] Moreover, the resulting discontinuous volume change leads to particle cracking, electrode degradation, and poor long-term cycling performance.[9] Finally, the lithium-ion ordering that tends to drive these transitions can reduce lithium-ion diffusivity, further slowing (de)insertion kinetics. Previous work has indicated that attenuation or complete suppression of miscibility gaps can enable fast Li insertion/extraction kinetics.[7,9]

One material system where fast charging/discharging has been enabled through suppression of phase transitions is MoO_2. Molybdenum(IV) dioxide is a rutile-like tunnel structure that has low electrical resistivity (8.8×10^{-5} Ω cm)[10,11] and facile Li diffusion parallel to the tunnels. Contrary to these positive attributes, bulk MoO_2 also undergoes a series of discontinuous phase transitions throughout cycling and consequently, shows slow Li insertion/extraction kinetics.[9,12] This set of characteristics makes MoO_2 an excellent model system to study the relationship between phase transitions and electrochemical performance. It has been previously shown by

Robertson *et al.* in a series of size-controlled samples that cycling kinetics are dramatically enhanced when the electrode material was nanostructured.[9] This improvement was correlated with a reduction of the observed miscibility gaps with decreasing particles size, with particles of 15 nm - 30 nm exhibiting completely continuous, solid-solution phase behavior. Moreover, it was found that nanostructured samples retained far more capacity over time, with 90% capacity retained after 1000 cycles compared to the 50% retained by their bulk counterparts. As impressive as these results are, nano-structuring as a general strategy can be impractical due to poor scale-up potential as well as increased electrical resistance and undesirable surface reactivity associated with the large increase in surface area to volume ratio.

An alternate route to controlling phase behavior and improving electrode performance is through the creation of solid solution electrode materials. Cation substitution in commercially relevant $LiNiO_2$ (LNO) and $LiFePO_4$ (LFP) to form solid solutions such as $LiNi_xMn_yCo_{1-x-y}O_2$ (NMC) and $LiMn_yFe_{1-y}PO_4$ is known to enhance high-rate capacity and cycle life.[7,13–15] This performance improvement is correlated with the shrinking or complete suppression of miscibility gaps during cycling, as observed in MoO_2 nanostructured systems. This increased range of Li miscibility is attributed to reduced transformation strain due to the competing structural demands of the different ions in solid solutions compared to pure analogues.[6,7] Within this framework, materials with different bonding types can show a broad range of behaviors. Ionic phases like LFP show almost entirely discontinuous phase behavior, which can be modulated by solid-solution formation. Layered transition metals oxides such as NMC contain mixtures of strong covalent metal-oxide bonds, and weaker Van der Waals gaps where the Li-ions reside. These materials not only differ in structure

type but also demonstrate less severe phase-transition behavior overall. Unfortunately, cation substation can make them prone to detrimental anti-site defects, which makes systematic study on the effect of cation substitution on phase behavior difficult.[16] The higher degree of covalent bonding in tunnel structured oxides like MoO_2 leads to different phase behavior with materials demonstrating multiple regimes of both continuous and discontinuous phase mechanisms. This makes the MoO_2 family and ideal platform for the study of solution-solution effects on intercalation induced phase transitions.

One topic of critical importance that is often ignored in the literature, is the degree of solid solution homogeneity on the nanoscale. The exact atomic ordering of a material can vary greatly. Based on both the inherent thermodynamics of mixing of constituent atoms and the kinetics of synthesis, compositions of mixed metal systems can range from entirely homogeneous, with completely random site occupancy, to discrete bulk domains of pure materials.[17,18] The exact degree of transition metal mixing affects both structural and electrochemical properties of the material. In particular, the introduction of cations with higher or lower electronegativity can alter the existing metal-oxygen covalency within the lattice via the inductive effect and thereby alter redox energies, and thus, redox voltage.[14] Additionally, cation substitution-induced alteration of bond length between metal and oxygen within a lattice can also alter metal-oxygen covalence, resulting in a change in redox potential.[14] Moreover, the extent of local phase separation can be difficult to detect through conventional bulk techniques such as XRD, with some reports suggesting that transition metal clustering on the order of 10 nm or less are undetectable through Bragg scattering.[17] In an idea explore further below, these subtle local structural

variations can be detected through the modulation of redox potentials and have the ability to dramatically alter Li-driven phase transitions.

In this work, we thus study the effect of cation substitution in MoO_2 tunnel structures by examining $Mo_{0.5}Nb_{0.5}O_2$ solid solutions with varying degrees of cation mixing, achieved through modification of synthesis precursors and parameters. According to Hume-Rothery's rules for solid solutions, solid solubility is substantially facilitated when the crystal structures of the dopant and matrix lattices are similar, ionic radii differences are ≤15%, cations have identical or near-identical valences, and cations have similar electronegativity.[19] Of the four criteria, NbO_2 satisfies three criteria: it has a similar rutile-like tunnel structure to MoO_2,[9,10,20] Nb^{4+} has a similar ionic radii of 0.68 Å compared to 0.65 Å for Mo^{4+},[21] and both atoms have identical cation valences. Thus, Nb is a suitable candidate for cation substitution within MoO_2.

In this work, we produced a family of $Mo_{0.5}Nb_{0.5}O_2$ materials with different degrees of cation mixing by synthesizing the materials at lower or higher temperatures, or by using molecular or cluster-based precursors. The electrochemical performance of all materials was measured, but a goal of understanding how solid solution formation affected lithium (de)insertion kinetics, and how redox peaks shifted with solid-solution formation. *Operando* X-ray diffraction (XRD) was then used to correlate structural evolution during Li insertion/extraction to changes in electrochemical performance characterized via cyclic voltammetry (CV) and galvanostatic cycling experiments.

Experimental Method

Synthesis of $Mo_{0.5}Nb_{0.5}O_2$ and Pure Phase NbO_2 and MoO_2 Powders

$Mo_{0.5}Nb_{0.5}O_2$ solid solutions and pure phase oxides (NbO_2 and MoO_2) were synthesized using either molecular chloride (Cl^-) precursors or a combination of polyoxometalate (POM) and oxalate precursors obtained from commercial suppliers without further purification.

For $Mo_{0.5}Nb_{0.5}O_2$ powders synthesized using Cl precursors, 287 mg of molybdenum(V) chloride (99.6 %, Alfa Aesar) and 284 mg of niobium(V) chloride (99.9 %, Thermo Scientific) were added to 6.0 ml of ethanol to create a solution with a 1:1 transition metal molar ratio. For pure phase NbO_2 powders, precursor solution was made by adding 568 mg of niobium(V) chloride (99.9 %, Thermo Scientific) to 6.0 ml of ethanol. These solutions were then dried at 80 °C to evaporate the ethanol. The resulting dried product from the $Mo_{0.5}Nb_{0.5}O_2$ precursor solution was then ground and calcined in a quartz boat in flowing forming gas mixture (95 % N_2, 5 % H_2) bubbled through deionized water at a gas flow rate of 0.0333 SLM. The purpose of water was to prevent over-reduction and formation of metallic phases. Calcination was carried out at three different temperatures: 650 °C (650 Cl), 850 °C (850 Cl), and 1050 °C (1050 Cl) with a 30-minute ramp time, 10-hour hold, and natural cooling rate to ambient temperature. The dried product from the NbO_2 precursor solution was ground and then calcined in a quartz boat in the same flowing forming gas mixture at a higher flow rate of 0.242 SLM, without being bubbled through water, at 1000 °C for 8 hours with a 30-minute ramp time and natural cooling rate to ambient temperature.

For $Mo_{0.5}Nb_{0.5}O_2$ powders synthesized using a combination of POM and oxalate precursors, 124 mg of ammonium molybdate (para) tetrahydrate, (99%, Alfa Aesar), and 225 mg of ammonium niobate(V) oxalate hydrate, (99.99 %, Sigma Aldrich), were added to 4.0 ml of deionized water to create a precursor solution. Pure phase MoO_2 precursor solution was synthesized in a similar way where 248 mg of ammonium molybdate (para) tetrahydrate, (99%, Alfa Aesar), was added to 4.0 ml of deionized water. The mixtures were heated to 60 °C and stirred with a magnetic stirrer until fully dissolved. This solution was then dried in an 80 °C oven to evaporate the water. The resulting dried product from the $Mo_{0.5}Nb_{0.5}O_2$ precursor solution was then ground and calcined under identical conditions as the Cl precursors at 850 °C (850 POM). Dried product from the MoO_2 was ground and calcined at 700 °C for 1 hour (20-minute ramp and natural cooling rate to ambient temperature) under a forming gas atmosphere bubbled through deionized water (0.092 SLM flow rate). All powders were stored in a glovebox with an inert atmosphere directly after calcination to prevent oxidation.

Structural Characterization

Both $Mo_{0.5}Nb_{0.5}O_2$ solid solution and pure phase powders were thoroughly ground in a mortar and pestle before structural characterization. Scanning electron microscope (SEM) images were acquired using a model NOVA 230 NanoSEM field-emission scanning electron microscope with a 7 kV accelerating voltage and 5.0 mm – 6.5 mm working distance. Sample purity and crystallographic information were obtained using laboratory X-ray diffraction (XRD) data collected with a PANalytical X'Pert Pro diffractometer operating with Cu Kα1 (λ = 1.5406 Å) using a 0.05° step size,

an accelerating voltage of 45 kV, and a current of 40 mA. X-ray diffraction data was processed using OriginPro 9.1.

Electrochemical Testing

Slurry Electrode Preparation

Both $Mo_{0.5}Nb_{0.5}O_2$ solid solution and pure phase powders (active material) were made into slurry-based electrodes for electrochemical characterization and testing. The active material, multiwalled carbon nanotube powder, vapor-grown carbon fiber powder, and 25 μm copper foil current collector (MTI Corporation) were dried at 100 °C under vacuum overnight. The dry powder components of the electrode were mixed and ground thoroughly in a mortar and pestle. A binder solution (2.5% wt % poly(vinylidene fluoride) (PVDF) in N-methylpyrrolidone (NMP)) was then added to the powder and mixed to form a homogenous slurry. The slurry was subsequently transferred onto copper foil and spread via doctor blading then dried at 100 °C under vacuum overnight. 1.0 cm^2 circular discs with an active mass loading of 1.0 – 1.5 mg were punched from the dried electrode sheets inside an inert atmosphere glovebox.

Coin Cell Assembly and Electrochemistry

The disc electrodes were assembled into stainless-steel 2032 coin cells (Landt) consisting of a stainless-steel conical spring, two 0.5 mm stainless-steel spacers and a glass fiber separator (Whatman) in between the disc electrode and a polished lithium metal disc acting as both a counter and reference electrode. The separator was wetted

with ~50 μL of electrolyte solution (1 M $LiPF_6$ in 1:1 ethylene carbonate:dimethyl carbonate, Sigma Aldrich).

All electrochemical techniques were conducted within 0.80 - 2.8 V except for the MoO_2 samples, which were cycled between 1.0 V – 2.8 V. Galvanostatic rate testing and long cycling experiments were conducted on a Landt Instruments Battery Test System CT3002A and an Arbin Instruments BT2000. C-rates for galvanostatic cycling were calculated based on a theoretical capacity of 212 mAh/g, which assumes 1 Li^+ insertion reaction into $Mo_{0.5}Nb_{0.5}O_2$, NbO_2, and MoO_2. Cyclic voltammetry experiments were performed using a Biologic VMP3 potentiostat.

Operando Synchrotron X-ray Diffraction

Pouch cells for *Operando* Synchrotron X-ray diffraction were constructed using nickel leads, glass fiber separators (Whatman), and aluminized mylar pouches. Li metal was used as counter and reference electrode. Approximately 50 μL of electrolyte (1.0 M $LiPF_6$ in 1:1 ethylene carbonate:dimethyl carbonate, Sigma Aldrich) was added into the pouch cells before they were sealed. *Operando* X-ray diffraction patterns of electrodes during cycling were taken at Stanford Synchrotron Radiation Lightsource Beamline 11-3 with 12.7 keV energy. Pouch cells were cycled with a Biologic VMP3 potentiostat at 0.5C for one full cycle before data collection. Cells were clamped between two plastic plates with thin X-ray windows to ensure both sufficient stack pressure during cycling, and sufficient X-ray penetration through the cell. All two-dimensional SXRD data were calibrated with a LaB_6 external standard and integrated into one-dimensional diffraction patterns using GSAS-II.[22] Diffraction of a blank pouch

cell (all components present but the working electrode material) was obtained and used for background subtraction to remove scattering from pouch cell components from the data.

Results and Discussion

Synthesis and Structural Characterization of $Mo_{0.5}Nb_{0.5}O_2$

A series of $Mo_{0.5}Nb_{0.5}O_2$ solid solutions were synthesized using metal chloride precursors at three different temperatures (650 °C, 850 °C, and 1050 °C) as well as POM and oxalate precursors at 850 °C. These temperatures were chosen to produce well mixed but poorly crystalline (650 Cl), well mixed and crystalline (850 Cl), and a phase separated and crystalline (1050 Cl) $Mo_{0.5}Nb_{0.5}O_2$ powder. High temperature was used to induce local phase separation in the sample. The $Mo_{0.5}Nb_{0.5}O_2$ sample synthesized with the POM and oxalate precursor (850 POM) was chosen to bias the sample towards local phase separation while retaining a similar degrees of crystallinity compared to 850 Cl sample. This is due to the fact that ammonium molybdate (para)tetrahydrate ($(NH_4)_6Mo_7O_{24}\cdot 4H_2O$) is a transition metal cluster, containing seven Mo atoms per molecule. This should favor formation of locally clustered domains of Mo-rich phases more readily than molecular Cl precursors, which contain only one transition metal per unit and should achieve good mixing of transition metals during the sol gel procedure used here. NbO_2 and MoO_2 pure phase powders were used as controls.

Samples were characterized via SEM and EDS (Figures 1A – 1K) to determine morphology and elemental composition. From the SEM imaging, it can be determined

that secondary particle sizes in all four samples are widely distributed. The smallest secondary particle sizes of the imaged samples are approximately 400 nm in diameter. However, largest secondary particle sizes imaged were anisotropic in shape and varied between different samples; they were approximately 4 μm for 650 Cl, and they were 10 μm for 850 Cl, 1050 Cl, and 850 POM. This suggests secondary particle coarsening in samples calcined at higher temperatures. Upon closer examination of the secondary particles, they appear to be constructed from smaller and more isotropic primary particles that are fused together. Primary particle sizes are estimated to be approximately 50 nm - 100 nm in 650 Cl and 850 Cl (Appendix figures A1A – A1B), 100 nm – 200 nm for 1050 Cl (Appendix figure A1C), and around 150 nm for 850 POM (Figure 1H). Increased primary particle sizes at higher temperatures may be a result of grain coarsening effects. Primary particles in samples made from Cl precursors (Figures 1E – 1G) appear to be more densely fused together than those made from POM precursors (Figure 1H), which are loosely connected to form a porous secondary particle structure. EDS mapping of all $Mo_{0.5}Nb_{0.5}O_2$ samples show a relatively homogenous distribution of Mo and Nb atoms throughout particles (Appendix figures A2, A3, A4, and A5).

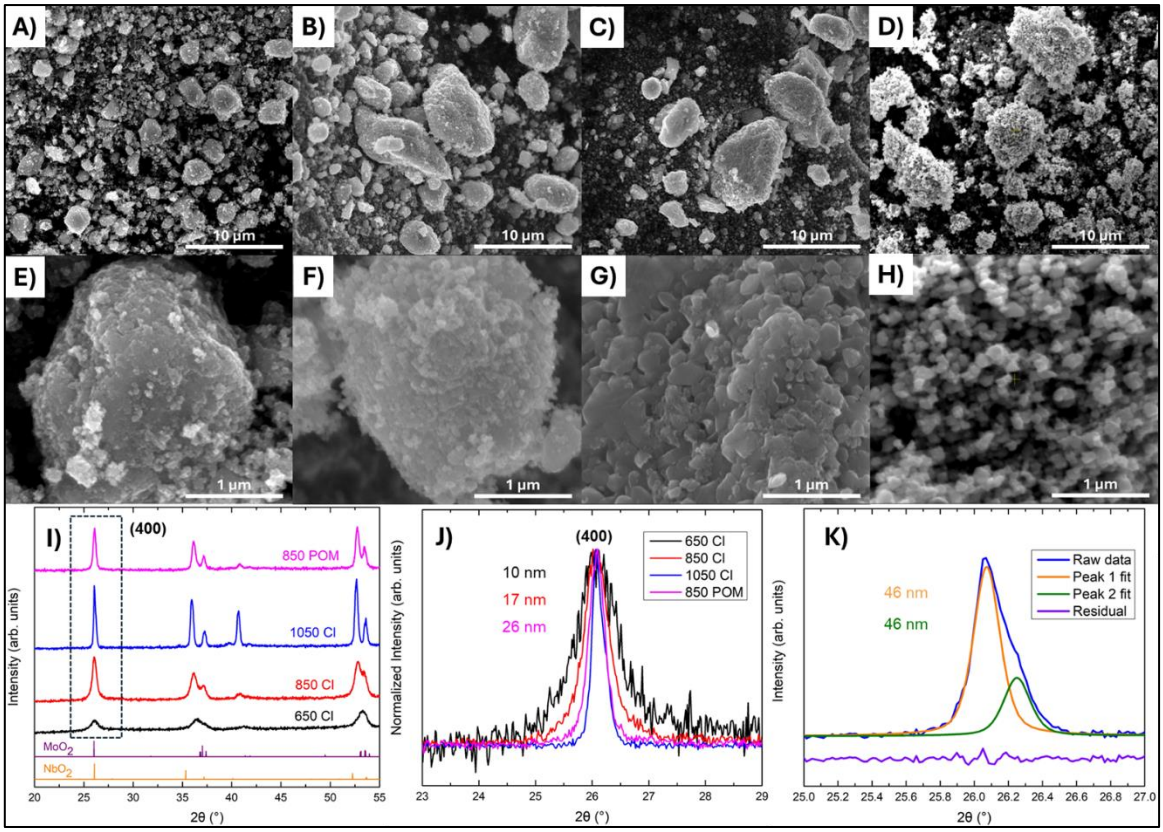

Figure 1: 5,000x magnification SEM images of: **(A)** 650 Cl, **(B)** 850 Cl, **(C)** 1050 Cl, and **(D)** 850 POM. 50,000x magnification SEM images of secondary particles: **(E)** 650 Cl, **(F)** 850 Cl, **(G)** 1050 Cl, and **(H)** 850 POM. **(I)** XRD patterns of $Mo_{0.5}Nb_{0.5}O_2$ synthesized at different conditions with MoO_2 (JCPDS 032-0671) and NbO_2 (JCPDS 076-0681) reference patterns. **(J)** The (400) reflections for all four samples studied in this work, and the calculated Scherrer sizes from that data for the 3 smallest domain size samples. **(K)** The (400) reflection of 1050 Cl sample, plotted with a double peak fit that was used to calculate a Scherrer size for this partly phase separate sample.

SEM images of pure phase NbO_2 and MoO_2 powders show much larger primary and secondary particles compared to $Mo_{0.5}Nb_{0.5}O_2$ solid solutions. Primary particles that form secondary particles in the NbO_2 sample are approximately 200 nm – 1 µm in diameter and secondary particles can be as big as 20 µm in diameter (Appendix figures A6A, A6B). On the other hand, SEM images of the MoO_2 samples (Appendix figures A7A, A7B) show faceted particles that are approximately 500 nm – 1.5 µm in width that do not appear to be a result of fused smaller primary particles like all the previously discussed samples.

Powder XRD patterns were used to confirm the crystal structure, evaluate crystallinity, calculate Scherrer sizes, and identify phase separation of the four different samples. Diffraction patterns show more resemblance to the NbO_2 reference pattern (JCPDS 076-0681) than to the MoO_2 reference pattern (JCPDS 032-0671) due to the presence of a reflection around 36° 2θ, which is absent in the MoO_2 reference pattern. Thus, reflections for the solid solutions in this work will be indexed to the NbO_2 reference pattern. The data obtained shows a prominent peak in the region corresponding to the (400) reflection (Figure 1I). This peak was used to qualitatively compare crystallinity as well as quantitatively calculate Scherrer sizes of the different samples (Figure 1J, 1K).[23] As expected, calcination temperature can be inversely correlated with peak broadness. The 650 Cl sample shows the broadest peak, suggesting that it is the least crystalline sample. It should be noted that for the same annealing conditions, the sample made with POM precursors (850 POM) appeared to be more crystalline than its Cl precursor counterpart (850 Cl). The 1050 Cl sample, which was calcined at the highest temperature, shows the narrowest peak, suggesting high crystallinity.[24,25] Scherrer sizes of 10 nm, 17 nm, and 26 nm for 650 Cl, 850 Cl, and 850 POM, respectively, also show an inverse correlation with peak broadness. Upon further scrutiny of the (400) peak from the 1050 Cl sample, it appears that peak is composed of two overlapping peaks (Figure 1K). The full peak shape can be well accounted for with two peaks, both corresponding to a Scherrer size of 46 nm. This suggests some macroscopic phase separation in the sample.

Electrochemical Characterization and Rate Performance

Cyclic voltammetry (CV) and galvanostatic rate cycling tests were used to evaluate the effects that the extent of solid solution mixing has on electrochemical performance of the $Mo_{0.5}Nb_{0.5}O_2$ system. To avoid the onset of MoO_2 conversion, the lower-bound voltage ranges were kept at 0.80 V for $Mo_{0.5}Nb_{0.5}O_2$ and 1.0 V for pure phase MoO_2, which is well above the conversion activation voltage of 0.16 V at room temperature reported in literature.[26] Conclusive evidence for conversion reactions have not been reported for NbO_2 in the limited studies on its applications in lithium battery electrodes, thus it can be assumed that the lower-bound voltage range of 0.8 V is sufficient to avoid conversion reactions in our system.[27–32] These tests were carried out under the assumption that all metal oxides discussed undergo a one electron reaction involving reversible insertion of one Li^+ ion (Equations 1 – 3). Therefore, the theoretical specific capacity for $Mo_{0.5}Nb_{0.5}O_2$, NbO_2, and MoO_2 are 212 mAh/g, 214 mAh/g, and 210 mAh/g, respectively.

$$Mo_{0.5}Nb_{0.5}O_2 + xe^- \rightleftharpoons Li_xMo_{0.5}Nb_{0.5}O_2 \quad (0 \leq x \leq 1) \qquad \textbf{(1)}$$

$$NbO_2 + xe^- \rightleftharpoons Li_xNbO_2 \quad (0 \leq x \leq 1) \qquad \textbf{(2)}$$

$$MoO_2 + xe^- \rightleftharpoons Li_xMoO_2 \quad (0 \leq x \leq 1) \qquad \textbf{(3)}$$

The extent of solid solution mixing/phase separation can be correlated to changes in peak separation and shape of the cyclic voltammograms. The 650 Cl sample, which is likely the most mixed but least crystalline sample, exhibits a slightly

boxy curve with multiple peaks with low definition (Figure 2A). Grey dashed lines in the figure trace identifiable peaks: Only one cathodic can be clearly identified at approximately 1.2 V while three anodic peaks were identified at approximately 1.7 V, 1.5 V, and 1.4 V. Thus, we were unable to match redox peak pairs for this sample. Unlike 650 Cl, the other samples show much more pronounced peaks and identifiable redox peak pairs. The sharper high voltage peak pairs are traced with black dashed lines and broader lower-voltage peak pairs are traced with grey dashed lines (Figure 2B, 2D, 2E). The difference of voltage between an anodic peak and its corresponding cathodic peak, also known as hysteresis or peak separation (ΔE_P), can be used as an indicator of fast or slow electrode kinetics.[33] It is generally accepted that lower peak-to-peak separation suggests fast reversible process, whereas larger peak separations are observed with sluggish electrode kinetics that may arise from phase nucleation and associated kinetic bottlenecks.[34,35] Peak separation values of both the high voltage and low voltage peaks were calculated using CV traces obtained at 1 mV/s scan rate (Figures 2C, 2F). The 850 Cl sample displayed the lowest peak separation, measuring 263 mV for the high voltage peak and 267 mV for the low voltage peak. In contrast, the 1050 Cl sample exhibited the largest separation values, with the high voltage peak at 353 mV and the low voltage peak at 414 mV. Positioned between these extremes, the 850 POM sample showcased intermediate peak separations, measuring 269 mV for the high voltage peak and 328 mV for the low voltage peak. In all, data from peak separation suggests that amongst the three samples that this analysis could be applied to, 850 Cl should be the kinetically the fastest material while 1050 Cl would be the slowest, leaving 850 POM situated in an intermediate position between the two.

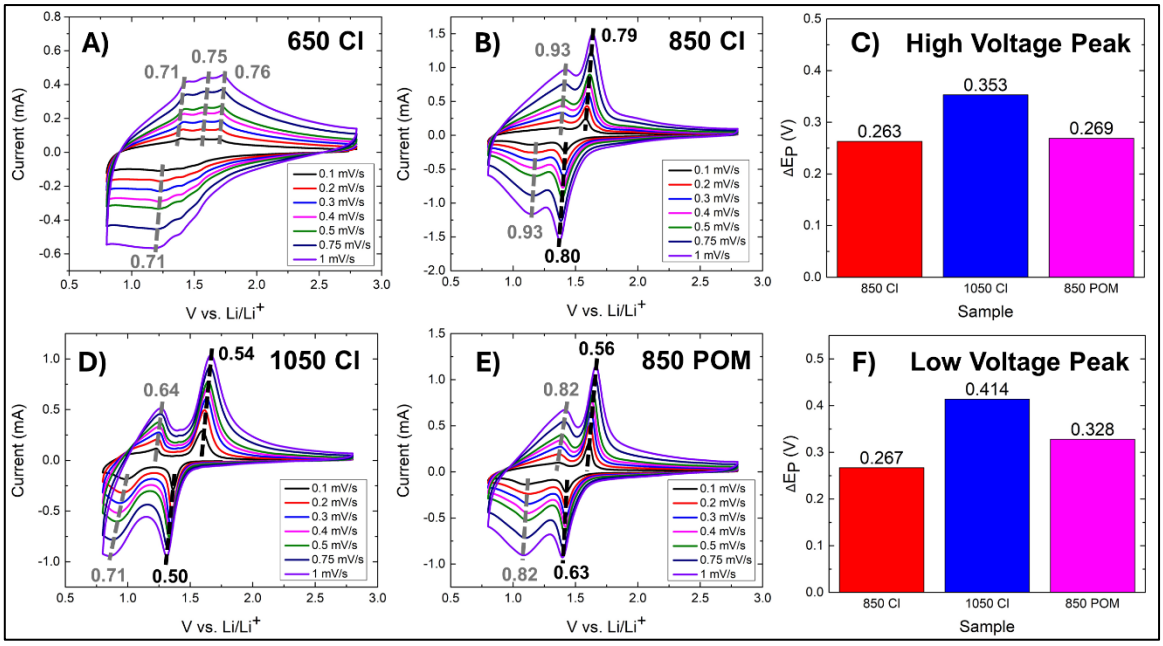

Figure 2: CV curves obtained at different scan rates and peak-specific b-values for: **(A)** 650 Cl, **(B)** 850 Cl, **(D)** 1050 Cl, and **(E)** 850 POM. Peak separation (ΔE_P) at 1 mV/s scan rate for the **(C)** High voltage peak (black dashed lines on CV curves) and **(F)** low voltage peak (grey dashed lines on CV curves).

Cyclic voltammograms can also be used to conduct b-value analysis, which assumes that the peak current (i_{peak} (A)) obeys a power-law relationship with varying sweep rate (v (mV/s)) according to the following equation:

$$i_{peak} = av^b \quad \textbf{(4)}$$

It is assumed that *a* and *b* are constants, thus, the value of b can be from the slope of a log(i_{peak}) vs. log(v) plot.[36–38] A value of 0.5 indicates that a reaction limited by semi-infinite diffusion (battery like) whilst a value of 1.0 indicates a capacitive current response not limited by diffusion (generally kinetically faster). Intermediate values suggest behavior that falls between semi-infinite diffusion and a purely capacitive response.[39–41] The b-values calculated for identifiable peaks in the collected CV curves suggests that the 850 Cl sample shows the most capacitive current response (b = 0.80, 0.79, 0.93, 0.93), the 650 Cl (b = 0.71, 0.76, 0.75, 0.71) and 850

POM materials (b = 0.63, 0.56, 0.82, 0.82) both lie in an intermediate regime, and that the 1050 Cl samples exhibits the most diffusion-limited current response (b = 0.5, 0.54, 0.71, 0.64). It is notable that the low-energy peaks in 850 Cl, 1050 Cl, and 850 POM all display higher b-values than the high-energy peaks, suggesting that less diffusion-hindered processes occur at lower voltage ranges. It is also worth noting that the CV curves for the poorly crystalline 650 Cl sample are fundamentally different in shape than those obtained for all other materials. While b-values were calculated at each identifiable redox peak, the peaks are very small, and sit atop a very broad background, suggesting that many processes contribute to the measured current, leading to complexity in interpreting the b-values.

To ascertain how the aforementioned conclusions on electrode kinetic behavior translate into performance in a battery electrode, the rate capabilities of the $Mo_{0.5}Nb_{0.5}O_2$ materials and pure phase controls were evaluated with galvanostatic rate testing (Figure 3A). Both MoO_2 and NbO_2 exhibited very poor performance, as demonstrated by the fact that their 0.5C capacities fell considerably short of the theoretical values. NbO_2 showed a particularly low capacity of only 29 mAh/g, while MoO_2 performed slightly better at 61 mAh/g. These discrepancies between experimental and theoretical capacities as well as poor performance compared to $Mo_{0.5}Nb_{0.5}O_2$ samples could be in part attributed to the larger primary particle sizes and thus, longer Li^+ diffusion lengths in the pure parent phases (Fig. A6 and A7). It should be noted, however, that the NbO_2 had a much smaller primary particles size but much worse cycling capacity than the MoO_2. In addition, for all the metal chloride-based samples, while the primary particles are relatively small, the secondary particle size is large and particles do not appear to be porous, suggesting is the secondary

particles size that should dominate the kinetics. Finally, NbO_2 is a poor conductor with a resistivity of approximately 10^4 Ω cm at room temperature.[42] Both the 850 Cl and 850 POM samples exhibit near theoretical capacities at 0.5C, with delithiation capacities of 210 mAh/g and 191 mAh/g, respectively (5th cycle). However, their capacity retention at higher rates diverges: At 20C (30th cycle), 850 Cl retains 62% of its 0.5C capacity (130 mAh/g), while 850 POM only retains 44% (84 mAh/g). This drop at high C rates for the 850 POM materials is even more noteworthy when one considers that the 850 POM material is the one sample with considerably smaller grain sizes compared to other samples, a fact that should facilitate high-rate kinetics. Conversely, 1050 Cl demonstrates sluggish cycling kinetics leading to low capacity that is particularly evident at high rates. With an initial 0.5C capacity of 159 mAh/g, which is significantly below the theoretical value, its performance worsens with increasing C-rates, retaining only 21% of its 0.5C capacity at 20C (33 mAh/g). These findings align with conclusions drawn from kinetic analysis of CV data.

The one sample that does not show the behavior expected based on its b-value is the 650 Cl material. At 0.5C, the 650 Cl sample demonstrated the poorest performance in terms of capacity achieved compared to the theoretical value, reaching only 123 mAh/g. Moreover, at 20C, it retained only 22% of its initial capacity (27 mAh/g). Studies pertaining to the effects of crystallinity on Li^+ diffusion and electrochemical performance suggest that lower crystallinity in crystal lattices (increased disorder) hinders the movement of Li^+ possibly due to the lack of migration paths.[43] Thus, the poor performance of 650 Cl may be attributed to its low crystallinity, as indicated by XRD data.

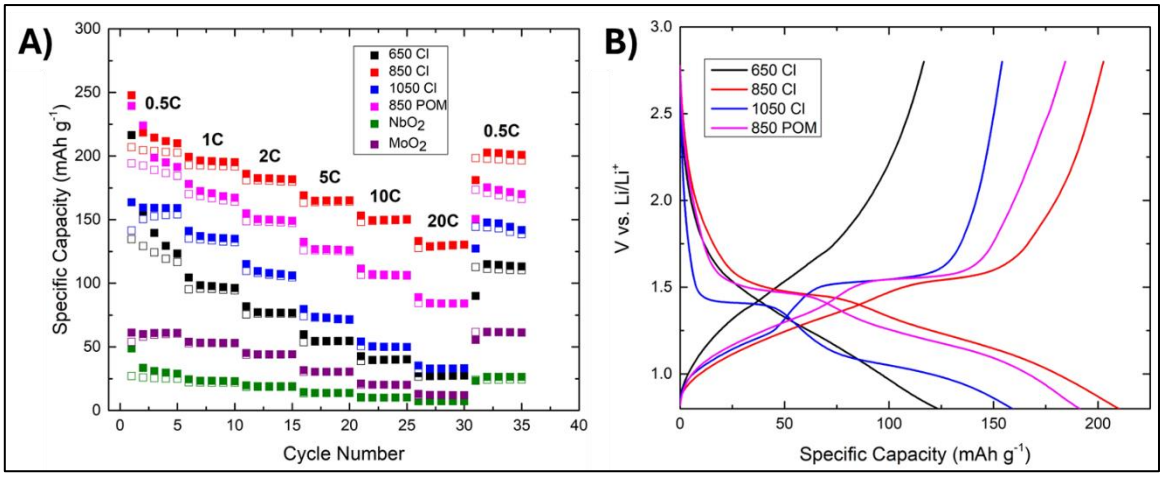

Figure 3: (A) Galvanostatic rate cycling performance at various C-rates; solid and open squares represent lithiation and delithiation capacity, respectively. **(B)** Galvanostatic profiles of the fifth cycle (0.5 C) for the various $Mo_{0.5}Nb_{0.5}O_2$ samples.

The differences in galvanostatic rate performance between the different $Mo_{0.5}Nb_{0.5}O_2$ samples are also reflected in their corresponding galvanostatic charge storage profiles. When considering the lithiation cycle (downward sloping profile), 1050 Cl shows a minimal amount of charge stored above 1.5 V (~7 mAh/g). A pronounced plateau region occurs around 1.4 V, followed by a sloping region until ~1.1 V, and then a less pronounced plateau region just above 1.0 V. In both the 850 Cl and 850 POM samples, the general shape of the profile remains similar, but they become more sloped, resulting in less pronounced plateaus. Up to about 30 mAh/g capacity is stored in the region above 1.5 V (approximately 40 and 30 mAh/g for 850 Cl and 850 POM, respectively). The first plateau for both samples occurs just below 1.5 V and the second plateau, while still present, is shorter and more noticeably sloped, and occurs at approximately 1.25 V. Both plateaus occur at higher voltage ranges than in the 1050 Cl sample. The 650 Cl sample had no identifiable plateaus either in the lithiation or delithiation cycles. Typically, plateau regions observed in a galvanostatic profile are associated with first-order phase transitions. This is because the coexistence of two

phases within a system pins the chemical potential, and therefore voltage, until the phase transition is complete.[13,44,45]

Structural Evolution Characterized via *Operando* XRD

To correlate the electrochemical performance of the $Mo_{0.5}Nb_{0.5}O_2$ systems with their structural evolution during Li insertion and extraction, *operando* XRD was carried out during galvanostatic cycling. These experiments were conducted using aluminized mylar pouch cells because its components attenuate the X-ray beam less than the stainless-steel components used in a 2032 coin cell, resulting in enhanced signal from the active electrode materials being analyzed. Figure 4 shows heat map-style plots tracing the evolution of the (400) reflection throughout a full lithiation/delithiation cycle as well as individual XRD scans within regions of interest.

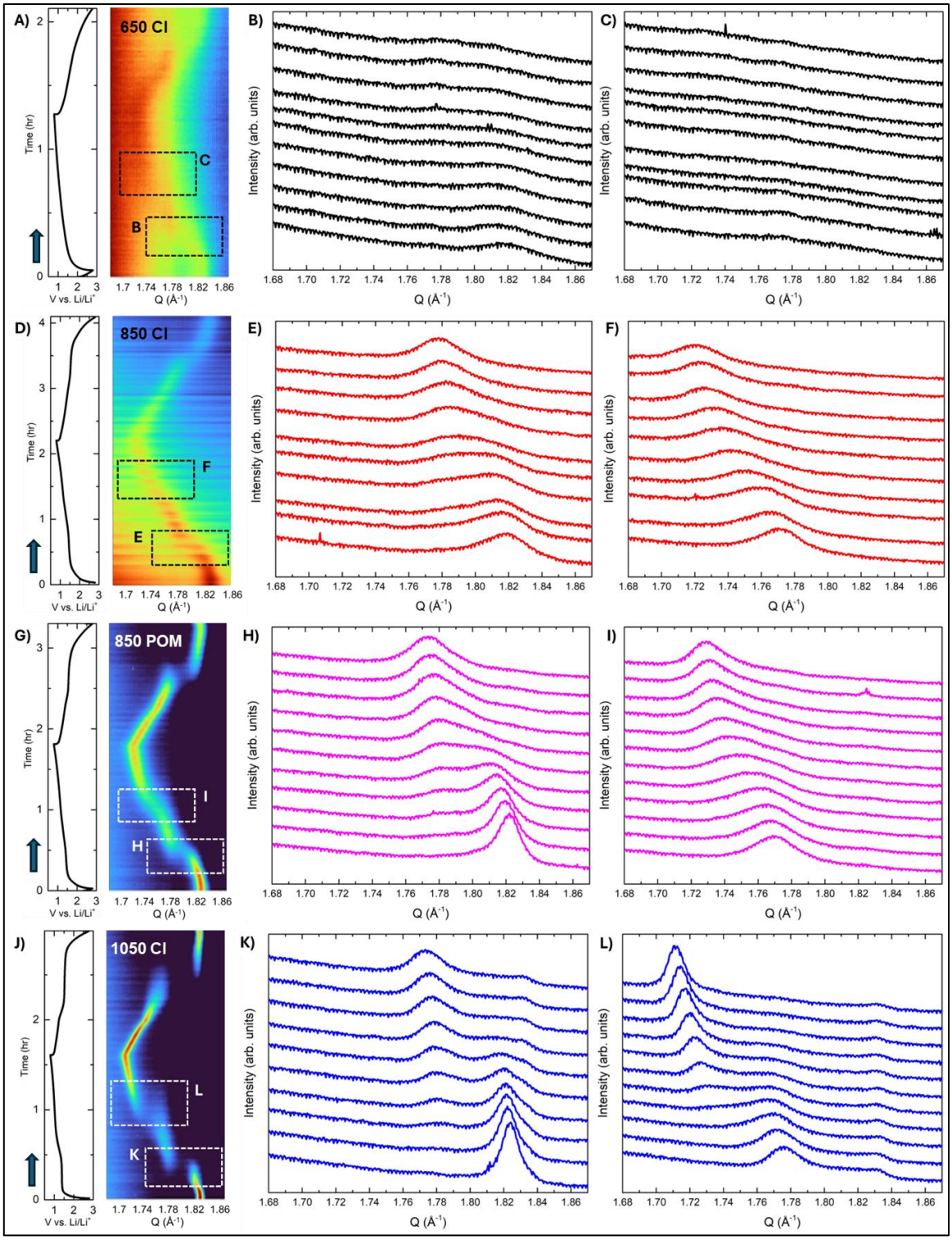

Figure 4: *Operando* XRD heat maps tracing the (400) reflection progression during cycling and the associated voltage profile of **(A)** 650 CI, **(D)** 850 CI, **(G)** 850 POM, and **(J)** 1050 CI samples. Waterfall plots **(B, C, E, F, H, I, K, L)** show individual scans of corresponding labelled regions in the heat maps.

Operando XRD heat-map of the 650 Cl sample (Figure A) displays broad peaks with low intensity, similar to the powder X-ray diffraction obtained for the sample, posing challenges in tracking their progression throughout the cycle. There is a possibility that the data indicates a trend of the peak position shifting towards lower Q values and broadening during lithiation. However, pinpointing the precise peak position becomes difficult, particularly in the latter phase of the lithiation cycle.

Throughout the lithiation cycle, the (400) peak in the 850 Cl sample (Figure 4D) also shifts towards lower Q values, consistent with lattice expansion as lithium is inserted. This peak broadens and then narrows as it shifts in the first region (Figure 4E) as well as the second region (Figure 4F). The voltage regions that these changes occur in correspond to the first (~1.5 V) and second (1.25 V) plateau regions identified in the GV traces (Figure 3B). Notably, fitting of the peak at the midpoint of the first region results in a single peak (Appendix figure A8A), suggesting a solid-solution mechanism of lithium insertion.[9] The behavior observed in the 850 POM sample (Figure 4G) was similar to that of the 850 Cl sample across both halves of the lithiation cycle (Figure 4H, 4I). However, fitting of the peak at the midpoint of the first region shows two-phase coexistence (Appendix figure A8B), with a miscibility gap of 0.028 $Å^{-1}$. On the other hand, the lower voltage region in the 850 Cl materials shows pure solid-solution behavior, and the 850 POM sample shows mostly solid-solution behavior with only a hint of peak broadening that cannot be well fit to extract a miscibility gap. This finding is in excellent agreement with the fact that the b-values for the lower voltage peak are much closer to 1 than those obtained for the low voltage peak, with a b-value of 0.92 for the 850 Cl material and a b-value of 0.82 for the 850 POM material. This detailed 1-to-1 correspondence between the phase behavior and the measured b-

value lends credence to the use of this analysis to determine pseudocapacitive behavior.

The heat-map of the 1050 Cl sample (Figure 4J) is drastically different compared to the previously discussed samples. Throughout the first half of the lithiation cycle (Figure 4K), the initial (400) peak shifts towards lower Q values, broadens, and then disappears within the voltage range corresponding to the high voltage peak and the first GV plateau region (~1.4 V). Concurrently, a peak emerges around 1.78 $Å^{-1}$. This indicates two-phase coexistence with a miscibility gap of 0.038 $Å^{-1}$ (Appendix figure A8C). In the latter half of the lithiation cycle (Figure 4L), the newly formed peak broadens and fades, while a third peak arises near 1.73 $Å^{-1}$, eventually shifting towards lower values as the lithiation cycle concludes. Here, the miscibility gap was calculated to be 0.032 $Å^{-1}$ (Appendix figure A8D). In agreement with the observed 2-phase coexistence, the b-values for all peaks in Figure 2D are much closer to 0.5. Interestingly, a small peak persists just above 1.83 $Å^{-1}$ throughout the entire lithiation cycle, which may correspond to a Nb-rich phase that shows little intercalation.

Overall, these data suggests that the phase separated 1050 Cl sample displays two distinct phase transitions corresponding to its two plateau regions witnessed in the GV profile, unlike the single-phase transition seen in 850 POM or the lack of distinct phase transitions in the 850 Cl and 650 Cl samples. The lower miscibility gap and absence of clear phase transitions in some materials correspond to enhanced electrode kinetics determined through CV analysis as well as to improved galvanostatic rate performance. However, the 650 Cl sample stands out as an outlier to this trend due to its inferior rate performance and the absence of observable phase

transitions. This deviation may be attributed to its poorly crystalline nature, as previously discussed.

Cycle-Life Performance

The effects of phase-behavior can also be correlated to cell cycle life for the $Mo_{0.5}Nb_{0.5}O_2$ materials (Figure 5). Lithiation capacity retention was calculated by comparison to the 2nd cycle. The 2nd cycle was used because after the five 0.1C formation cycles, every sample showed an anomalously high 1st cycle capacity, and thus, the 2nd cycle can be considered a more accurate representation of 2C capacity. The 1050 CI material shows the worst cycle life with 58 % capacity retention after 200 cycles and 54 % after 300 cycles. This is followed closely by 850 POM sample, with 60 % capacity retention after 200 cycles and 55 % after 300 cycles. In comparison to these two samples, the 850 CI material showed excellent capacity retention, with 73 % and 68 % of its initial capacity retained after 200 and 300 cycles respectively. The 650 CI material starts as a very low capacity of 79.6 mAh/g but shows the least capacity decay: 94 % retention at 200 cycles and 91 % at 300 cycles.

These results suggest that cycle life and capacity retention are directly related to the presence of a phase transition and the size of the miscibility gap. Specifically, the 1050 CI material exhibited two distinct phase transitions and the widest miscibility gap, resulting in the poorest capacity retention. The 850 POM material displayed only one phase transition and a smaller miscibility gap in comparison to the 1050 CI sample, leading to slightly better performance. Notably, both the 850 CI and 650 CI samples demonstrated no clear phase transitions while, demonstrating the best capacity

retention. However, it's worth noting that 650 Cl displayed the lowest starting capacity among the materials examined, and it is easier to retain capacity when cycling to very low capacity. These observations corroborate conclusions in previous literature where it has been reported that strain and volume expansion induced by phase transitions contribute to particle cracking over time, and thus, negatively impact long-term cycle life.[46–49]

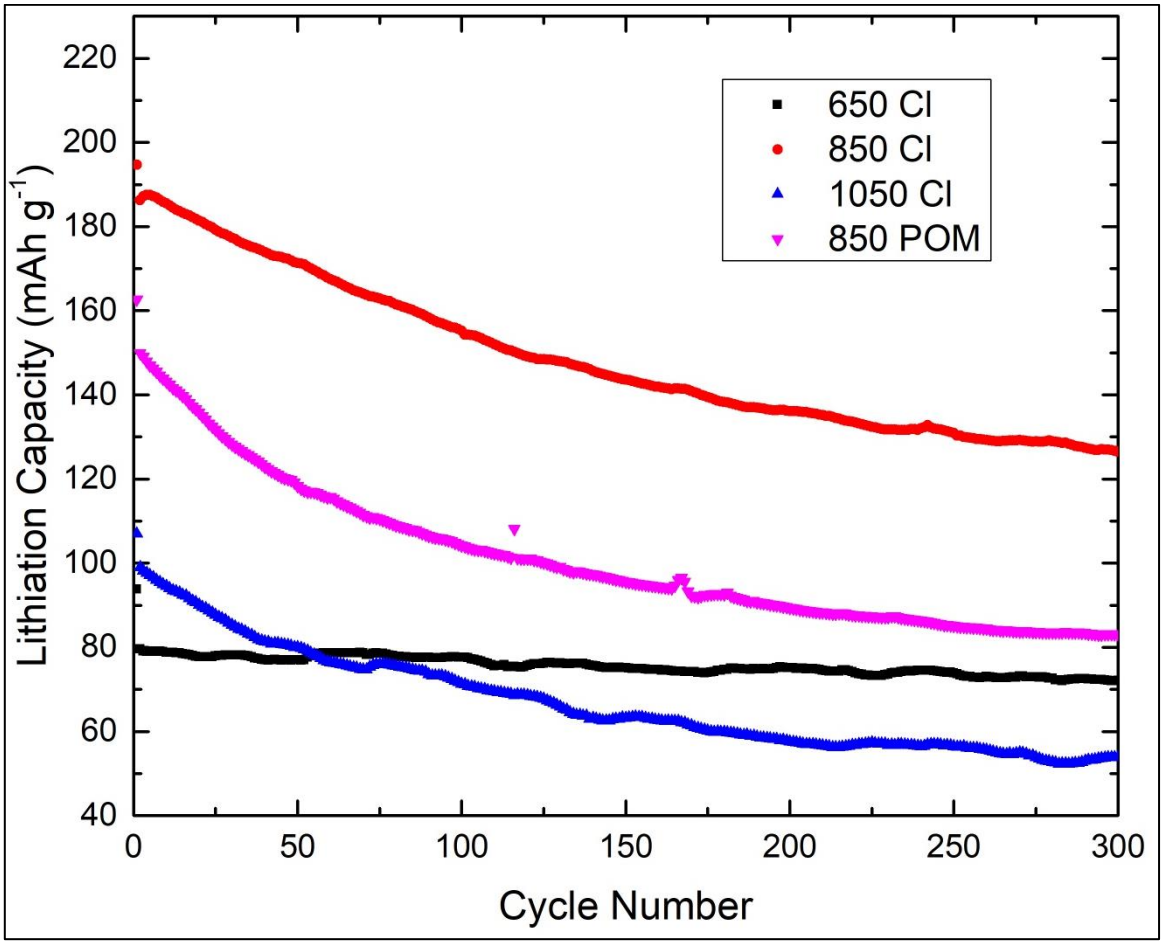

Figure 5: Long-term galvanostatic cycling performance for the different $Mo_{0.5}Nb_{0.5}O_2$ materials at 2C. Five 0.1C formation cycles were completed before commencement of the test for all samples.

Conclusion

By utilizing both precursor choice and annealing temperature to vary the degree of mixing in $Mo_{0.5}Nb_{0.5}O_2$ solid solutions, coupled with *operando* XRD and electrochemical characterization, this work has demonstrated the effect that ion mixing has on phase transition suppression in tunnel-like rutile structures during lithiation/delithiation and its correlation with improved electrochemical performance. Through *operando* XRD, it is evident that the poorly crystalline, but well-mixed electrode material (650 CI) and crystalline well-mixed electrode material (850 CI) both show suppressed first-order phase transitions during lithiation, while clustered (850 POM) and phase separated (1050 CI) materials both show distinct first-order phase transitions. For these partly phase separated samples, the size of the miscibility gap in the initial Li-insertion-induced first-order phase transition increases with increasing phase separation. Aside from the poorly crystalline mixed electrode (650 CI), which displayed poor electrochemical rate performance, likely due to poor Li mobility in the poorly crystalline structure, phase-transition suppression in well-mixed materials resulted in improved cycling rate performance: the 850 CI material stores 130 mAh/g (62 % of 0.5C capacity) at 20C, whereas the 850 POM sample stores only 84 mAh/g (44 % of 0.5C capacity) at 20C, and the 1050 CI sample stores a mere 33 mAh/g (21% of 0.5C capacity) at 20C.

Finally, long-term cycling shows a drastic difference in cycle life between electrodes with and without suppressed first-order phase transitions: The mixed 850 CI sample retained 73 % of its initial capacity after 300 cycles, a stark contrast compared to the clustered 850 CI and phase separated 1050 CI samples which retained only 60 % and 58 % after of their initial capacities after 200 cycles. Overall,

the fact that the crystalline mixed 850 Cl sample shows a mostly suppressed first-order phase transition during lithiation/delithiation, instead of the distinct first-order phase transitions that occur in the clustered 850 POM and phase separated 1050 Cl samples, favorably impacts all aspects of cycling kinetics and longevity.

Appendix

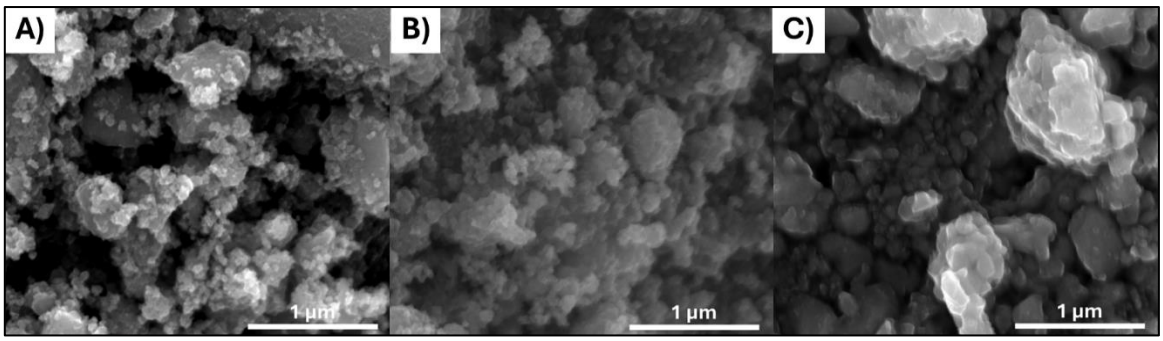

Figure A1: 50,000x magnification SEM images of loose particles: **(A)** 650 Cl, **(B)** 850 Cl, and **(C)** 1050 Cl.

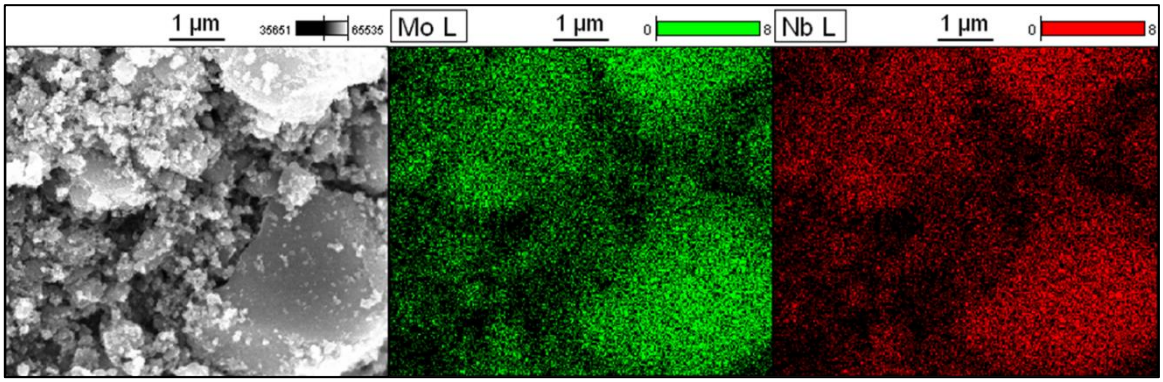

Figure A2: EDS elemental mapping showing Mo (green) and Nb (red) in 650 Cl.

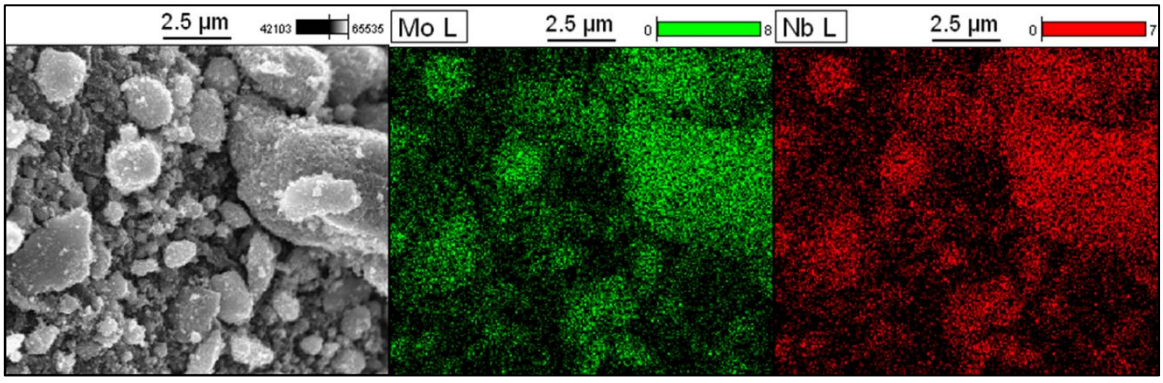

Figure A3: EDS elemental mapping showing Mo (green) and Nb (red) in 850 Cl.

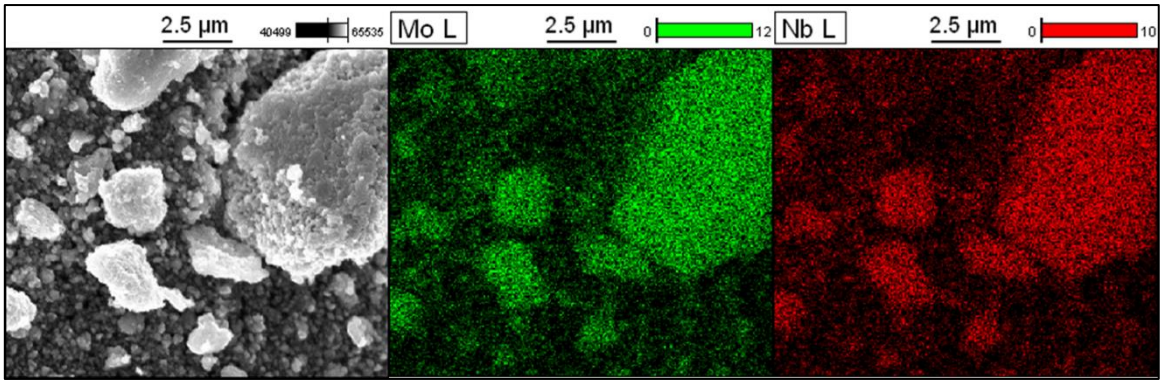

Figure A4: EDS elemental mapping showing Mo (green) and Nb (red) in 1050 Cl.

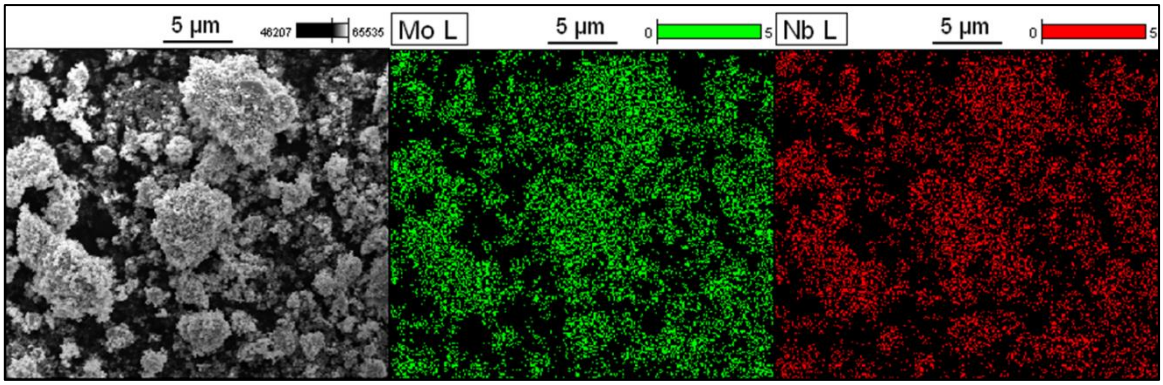

Figure A5: EDS elemental mapping showing Mo (green) and Nb (red) in 850 POM.

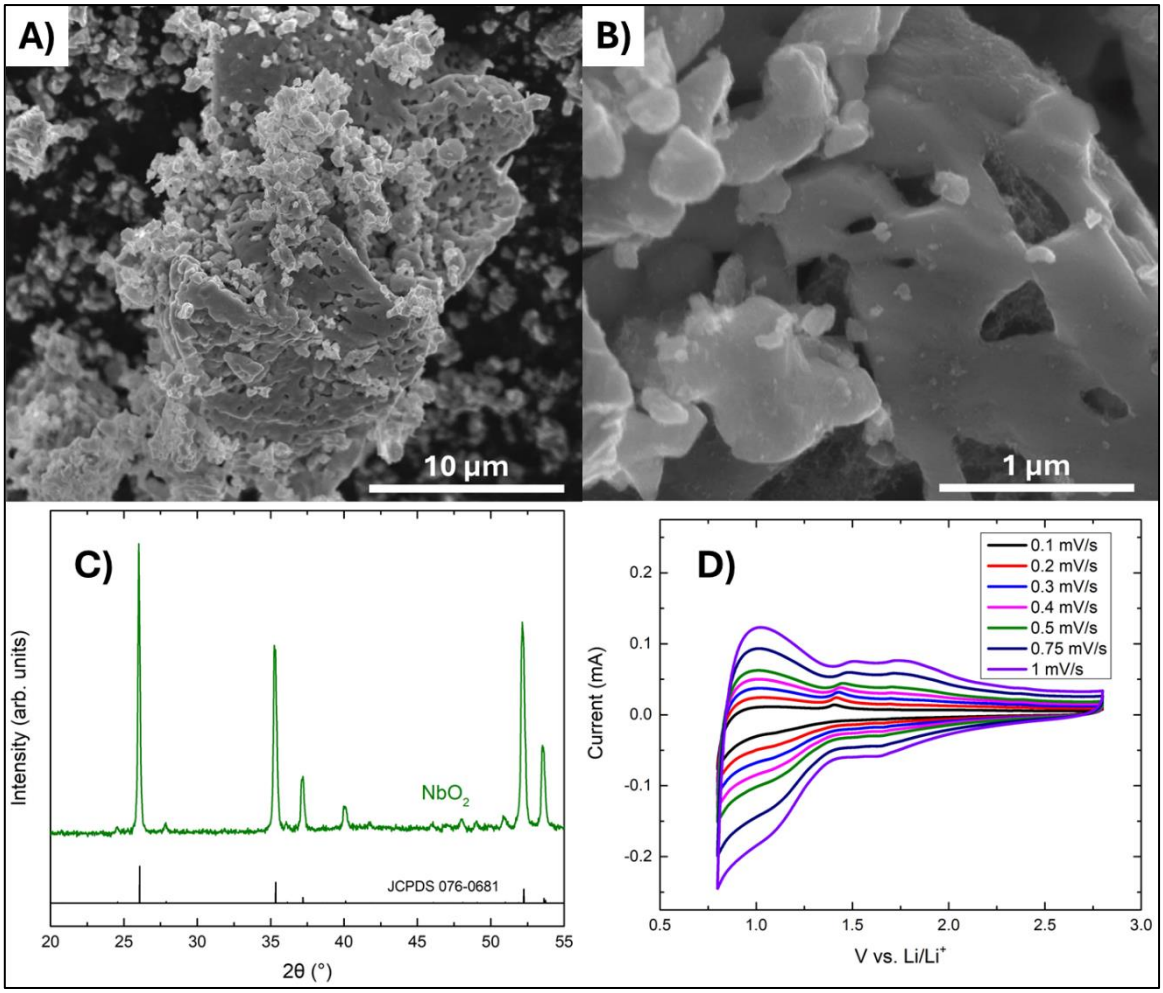

Figure A6: (A) 5,000x magnification and **(B)** 50,000x magnification SEM images of NbO_2. **(C)** XRD pattern of powder NbO_2. **(D)** CV curves of NbO_2 electrodes.

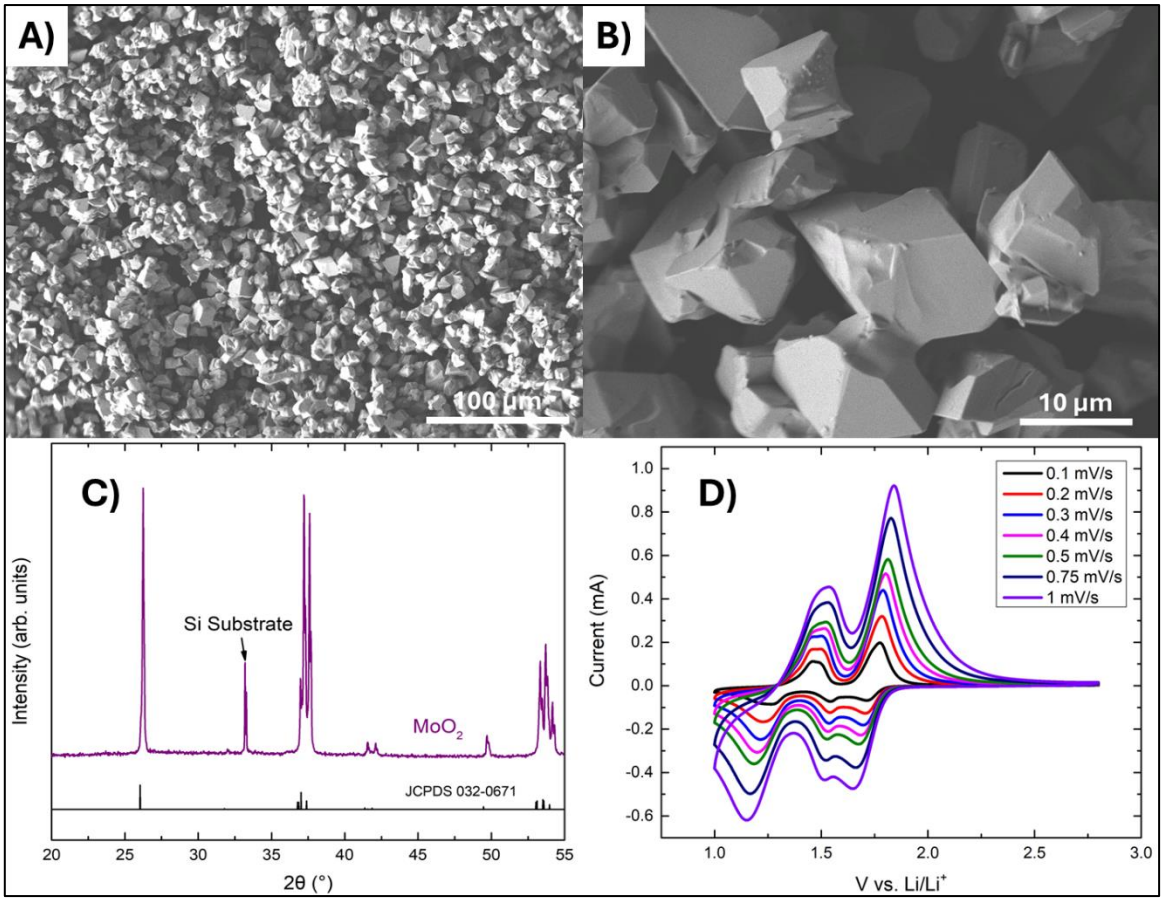

Figure A7: (A) 300x magnification and **(B)** 2,300x magnification SEM images of MoO_2. **(C)** XRD pattern of powder MoO_2 taken on a silicon substrate. **(D)** CV curves of MoO_2 electrodes.

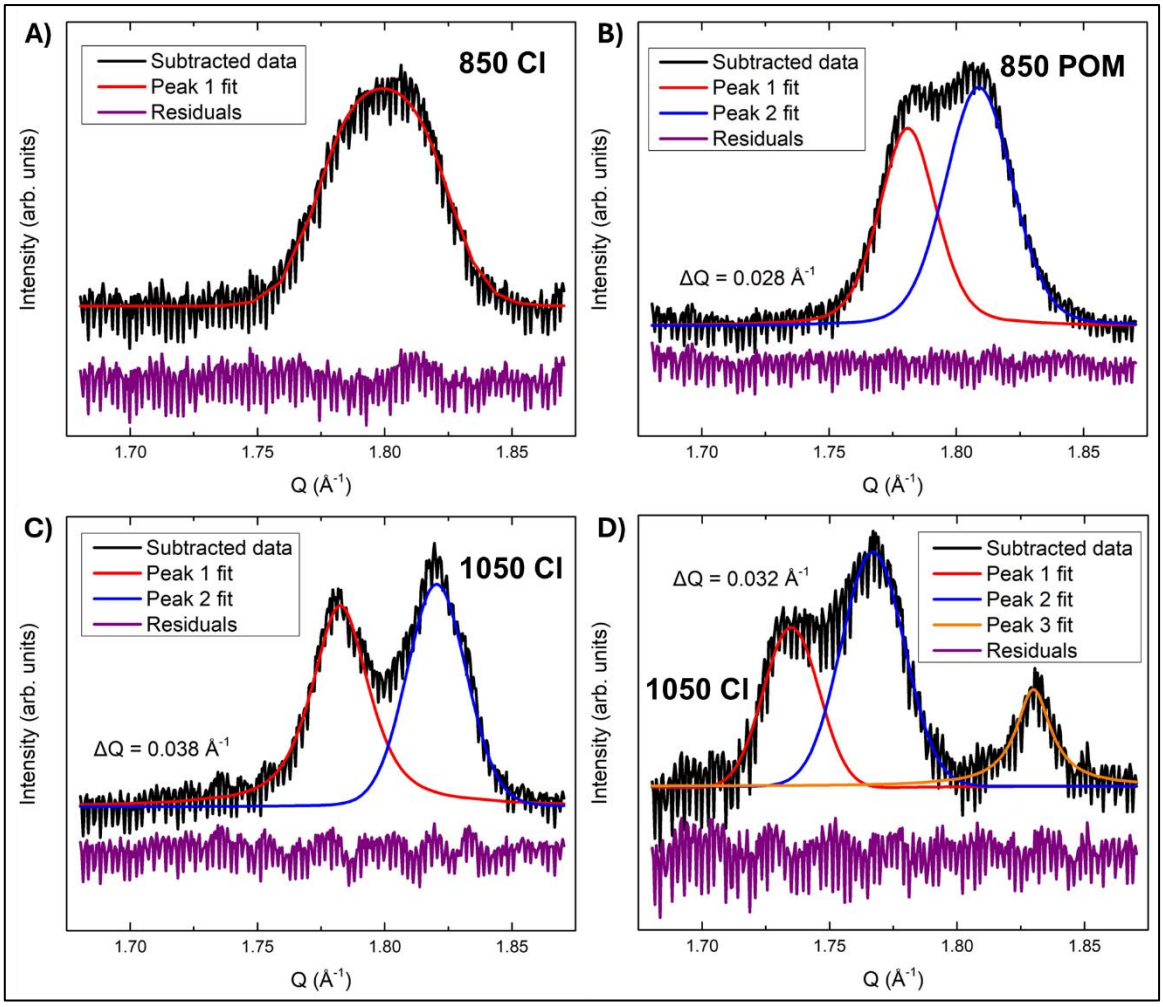

Figure A8: Subtracted data and fitted peaks of XRD scans at the midpoint of: **(A)** 850 Cl first phase transition, **(B)** 850 POM first phase transition, **(C)** 1050 Cl first phase transition, and **(D)** 1050 Cl second phase transition. Calculated miscibility gaps (ΔQ) between the fits of peak 1 and 2 are stated within the panels.

References

(1) Heubner, C.; Nikolowski, K.; Reuber, S.; Schneider, M.; Wolter, M.; Michaelis, A. Recent Insights into Rate Performance Limitations of Li-Ion Batteries. *Batter. Supercaps* **2021**, *4* (2), 268–285. https://doi.org/10.1002/batt.202000227.

(2) Wassiliadis, N.; Schneider, J.; Frank, A.; Wildfeuer, L.; Lin, X.; Jossen, A.; Lienkamp, M. Review of Fast Charging Strategies for Lithium-Ion Battery Systems and Their Applicability for Battery Electric Vehicles. *J. Energy Storage* **2021**, *44*, 103306. https://doi.org/10.1016/j.est.2021.103306.

(3) Deng, D. Li-Ion Batteries: Basics, Progress, and Challenges. *Energy Sci. Eng.* **2015**, *3* (5), 385–418. https://doi.org/10.1002/ese3.95.

(4) Tomaszewska, A.; Chu, Z.; Feng, X.; O'Kane, S.; Liu, X.; Chen, J.; Ji, C.; Endler, E.; Li, R.; Liu, L.; Li, Y.; Zheng, S.; Vetterlein, S.; Gao, M.; Du, J.; Parkes, M.; Ouyang, M.; Marinescu, M.; Offer, G.; Wu, B. Lithium-Ion Battery Fast Charging: A Review. *eTransportation* **2019**, *1*, 100011. https://doi.org/10.1016/j.etran.2019.100011.

(5) Weiss, M.; Ruess, R.; Kasnatscheew, J.; Levartovsky, Y.; Levy, N. R.; Minnmann, P.; Stolz, L.; Waldmann, T.; Wohlfahrt-Mehrens, M.; Aurbach, D.; Winter, M.; Ein-Eli, Y.; Janek, J. Fast Charging of Lithium-Ion Batteries: A Review of Materials Aspects. *Adv. Energy Mater.* **2021**, *11* (33), 2101126. https://doi.org/10.1002/aenm.202101126.

(6) Meethong, N.; Huang, H.-Y. S.; Speakman, S. A.; Carter, W. C.; Chiang, Y.-M. Strain Accommodation during Phase Transformations in Olivine-Based Cathodes as a Materials Selection Criterion for High-Power Rechargeable Batteries. *Adv. Funct. Mater.* **2007**, *17* (7), 1115–1123. https://doi.org/10.1002/adfm.200600938.

(7) Ravnsbæk, D. B.; Xiang, K.; Xing, W.; Borkiewicz, O. J.; Wiaderek, K. M.; Gionet, P.; Chapman, K. W.; Chupas, P. J.; Tang, M.; Chiang, Y.-M. Engineering the Transformation Strain in LiMnyFe1–yPO4 Olivines for Ultrahigh Rate Battery Cathodes. *Nano Lett.* **2016**, *16* (4), 2375–2380. https://doi.org/10.1021/acs.nanolett.5b05146.

(8) Liu, H.; Strobridge, F. C.; Borkiewicz, O. J.; Wiaderek, K. M.; Chapman, K. W.; Chupas, P. J.; Grey, C. P. Capturing Metastable Structures during High-Rate Cycling of LiFePO4 Nanoparticle Electrodes. *Science* **2014**, *344* (6191), 1252817. https://doi.org/10.1126/science.1252817.

(9) Robertson, D. D.; Cumberbatch, H.; Pe, D. J.; Yao, Y.; Tolbert, S. H. Understanding How the Suppression of Insertion-Induced Phase Transitions Leads to Fast Charging in Nanoscale LixMoO2. *ACS Nano* **2024**, *18* (1), 996–1012. https://doi.org/10.1021/acsnano.3c10169.

(10) Rogers, D. B.; Shannon, R. D.; Sleight, A. W.; Gillson, J. L. Crystal Chemistry of Metal Dioxides with Rutile-Related Structures. *Inorg. Chem.* **1969**, *8* (4), 841–849. https://doi.org/10.1021/ic50074a029.

(11) Fang, X.; Guo, B.; Shi, Y.; Li, B.; Hua, C.; Yao, C.; Zhang, Y.; Hu, Y.-S.; Wang, Z.; Stucky, G. D.; Chen, L. Enhanced Li Storage Performance of Ordered Mesoporous MoO2viatungsten Doping. *Nanoscale* **2012**, *4* (5), 1541–1544. https://doi.org/10.1039/C2NR12017H.

(12) Dahn, J. R.; McKinnon, W. R. Structure and Electrochemistry of LixMoO2. *Solid State Ion.* **1987**, *23* (1), 1–7. https://doi.org/10.1016/0167-2738(87)90074-9.

(13) Tang, M.; Carter, W. C.; Chiang, Y.-M. Electrochemically Driven Phase Transitions in Insertion Electrodes for Lithium-Ion Batteries: Examples in Lithium Metal Phosphate Olivines. *Annu. Rev. Mater. Res.* **2010**, *40* (Volume 40, 2010), 501–529. https://doi.org/10.1146/annurev-matsci-070909-104435.

(14) Muraliganth, T.; Manthiram, A. Understanding the Shifts in the Redox Potentials of Olivine LiM1−yMyPO4 (M = Fe, Mn, Co, and Mg) Solid Solution Cathodes. *J. Phys. Chem. C* **2010**, *114* (36), 15530–15540. https://doi.org/10.1021/jp1055107.

(15) Omenya, F.; Chernova, N. A.; Zhang, R.; Fang, J.; Huang, Y.; Cohen, F.; Dobrzynski, N.; Senanayake, S.; Xu, W.; Whittingham, M. S. Why Substitution Enhances the Reactivity of LiFePO4. *Chem. Mater.* **2013**, *25* (1), 85–89. https://doi.org/10.1021/cm303259j.

(16) Li, J.; Liang, G.; Zheng, W.; Zhang, S.; Davey, K.; Pang, W. K.; Guo, Z. Addressing Cation Mixing in Layered Structured Cathodes for Lithium-Ion Batteries: A Critical Review. *Nano Mater. Sci.* **2023**, *5* (4), 404–420. https://doi.org/10.1016/j.nanoms.2022.09.001.

(17) Michaelsen, C. On the Structure and Homogeneity of Solid Solutions: The Limits of Conventional X-Ray Diffraction. *Philos. Mag. A* **1995**, *72* (3), 813–828. https://doi.org/10.1080/01418619508243802.

(18) He, J. H.; Sheng, H. W.; Lin, J. S.; Schilling, P. J.; Tittsworth, R. C.; Ma, E. Homogeneity of a Supersaturated Solid Solution. *Phys. Rev. Lett.* **2002**, *89* (12), 125507. https://doi.org/10.1103/PhysRevLett.89.125507.

(19) Chen, W.-F.; Chen, H.; Koshy, P.; Nakaruk, A.; Sorrell, C. C. Effect of Doping on the Properties and Photocatalytic Performance of Titania Thin Films on Glass Substrates: Single-Ion Doping with Cobalt or Molybdenum. *Mater. Chem. Phys.* **2018**, *205*, 334–346. https://doi.org/10.1016/j.matchemphys.2017.11.021.

(20) Zhang, J.; Norris, K. J.; Gibson, G.; Zhao, D.; Samuels, K.; Zhang, M. M.; Yang, J. J.; Park, J.; Sinclair, R.; Jeon, Y.; Li, Z.; Williams, R. S. Thermally Induced Crystallization in NbO2 Thin Films. *Sci. Rep.* **2016**, *6* (1), 34294. https://doi.org/10.1038/srep34294.

(21) Shannon, R. D. Revised Effective Ionic Radii and Systematic Studies of Interatomic Distances in Halides and Chalcogenides. *Acta Crystallogr. A* **1976**, *32* (5), 751–767. https://doi.org/10.1107/S0567739476001551.

(22) Toby, B. H.; Von Dreele, R. B. GSAS-II: The Genesis of a Modern Open-Source All Purpose Crystallography Software Package. *J. Appl. Crystallogr.* **2013**, *46* (2), 544–549. https://doi.org/10.1107/S0021889813003531.

(23) Holder, C. F.; Schaak, R. E. Tutorial on Powder X-Ray Diffraction for Characterizing Nanoscale Materials. *ACS Nano* **2019**, *13* (7), 7359–7365. https://doi.org/10.1021/acsnano.9b05157.

(24) Chauhan, A. Powder XRD Technique and Its Applications in Science and Technology. *J. Anal. Bioanal. Tech.* **2014**, *5* (6). https://doi.org/10.4172/2155-9872.1000212.

(25) West, A. R. *Solid State Chemistry and Its Applications*, Second Edition, Student Edition.; John Wiley & Sons, Ltd, 2014.

(26) Ku, J. H.; Jung, Y. S.; Lee, K. T.; Kim, C. H.; Oh, S. M. Thermoelectrochemically Activated MoO2 Powder Electrode for Lithium Secondary Batteries. *J. Electrochem. Soc.* **2009**, *156* (8), A688. https://doi.org/10.1149/1.3141670.

(27) Park, H.; Lee, D.; Song, T. High Capacity Monoclinic Nb2O5 and Semiconducting NbO2 Composite as High-Power Anode Material for Li-Ion Batteries. *J. Power Sources* **2019**, *414*, 377–382. https://doi.org/10.1016/j.jpowsour.2019.01.015.

(28) Chithaiah, P.; Sahoo, R. C.; Seok, J. H.; Lee, S. U.; Matte, H. S. S. R.; Rao, C. N. R. NbO2 a Highly Stable, Ultrafast Anode Material for Li- and Na-Ion Batteries. *ACS Appl. Mater. Interfaces* **2023**, *15* (39), 45868–45875. https://doi.org/10.1021/acsami.3c08694.

(29) Kim, Y.-S.; Cho, Y.; Nogales, P. M.; Jeong, S.-K. NbO2 as a Noble Zero-Strain Material for Li-Ion Batteries: Electrochemical Redox Behavior in a Nonaqueous Solution. *Energies* **2019**, *12* (15), 2960. https://doi.org/10.3390/en12152960.

(30) Asfaw, H. D.; Tai, C.-W.; Nyholm, L.; Edström, K. Over-Stoichiometric NbO2 Nanoparticles for a High Energy and Power Density Lithium Microbattery. *ChemNanoMat* **2017**, *3* (9), 646–655. https://doi.org/10.1002/cnma.201700141.

(31) Cho, Y. H.; Jeong, S. K.; Kim, Y. S. Electrochemical Properties of Chemically Etched-NbO2 as a Negative Electrode Material for Lithium Ion Batteries. *Adv. Mater. Res.* **2015**, *1120–1121*, 115–118. https://doi.org/10.4028/www.scientific.net/AMR.1120-1121.115.

(32) Kong, L.; Zhang, C.; Wang, J.; Qiao, W.; Ling, L.; Long, D. Nanoarchitectured Nb2O5 Hollow, Nb2O5@carbon and NbO2@carbon Core-Shell Microspheres for Ultrahigh-Rate Intercalation Pseudocapacitors. *Sci. Rep.* **2016**, *6* (1), 21177. https://doi.org/10.1038/srep21177.

(33) Streeter, I.; Wildgoose, G. G.; Shao, L.; Compton, R. G. Cyclic Voltammetry on Electrode Surfaces Covered with Porous Layers: An Analysis of Electron Transfer

Kinetics at Single-Walled Carbon Nanotube Modified Electrodes. *Sens. Actuators B Chem.* **2008**, *133* (2), 462–466. https://doi.org/10.1016/j.snb.2008.03.015.

(34) Lee, Y.-T.; Kuo, C.-T.; Yew, T.-R. Investigation on the Voltage Hysteresis of Mn3O4 for Lithium-Ion Battery Applications. *ACS Appl. Mater. Interfaces* **2021**, *13* (1), 570–579. https://doi.org/10.1021/acsami.0c18368.

(35) Yao, Z.; Kim, S.; Aykol, M.; Li, Q.; Wu, J.; He, J.; Wolverton, C. Revealing the Conversion Mechanism of Transition Metal Oxide Electrodes during Lithiation from First-Principles. *Chem. Mater.* **2017**, *29* (21), 9011–9022. https://doi.org/10.1021/acs.chemmater.7b02058.

(36) Yang, X.; Rogach, A. L. Electrochemical Techniques in Battery Research: A Tutorial for Nonelectrochemists. *Adv. Energy Mater.* **2019**, *9* (25), 1900747. https://doi.org/10.1002/aenm.201900747.

(37) Augustyn, V.; Come, J.; Lowe, M. A.; Kim, J. W.; Taberna, P.-L.; Tolbert, S. H.; Abruña, H. D.; Simon, P.; Dunn, B. High-Rate Electrochemical Energy Storage through Li+ Intercalation Pseudocapacitance. *Nat. Mater.* **2013**, *12* (6), 518–522. https://doi.org/10.1038/nmat3601.

(38) Lindström, H.; Södergren, S.; Solbrand, A.; Rensmo, H.; Hjelm, J.; Hagfeldt, A.; Lindquist, S.-E. Li+ Ion Insertion in TiO2 (Anatase). 2. Voltammetry on Nanoporous Films. *J. Phys. Chem. B* **1997**, *101* (39), 7717–7722. https://doi.org/10.1021/jp970490q.

(39) van den Bergh, W.; Lokupitiya, H. N.; Vest, N. A.; Reid, B.; Guldin, S.; Stefik, M. Nanostructure Dependence of T-Nb2O5 Intercalation Pseudocapacitance Probed Using Tunable Isomorphic Architectures. *Adv. Funct. Mater.* **2021**, *31* (1), 2007826. https://doi.org/10.1002/adfm.202007826.

(40) Cook, J. B.; Lin, T. C.; Kim, H.-S.; Siordia, A.; Dunn, B. S.; Tolbert, S. H. Suppression of Electrochemically Driven Phase Transitions in Nanostructured MoS2 Pseudocapacitors Probed Using Operando X-Ray Diffraction. *ACS Nano* **2019**, *13* (2), 1223–1231. https://doi.org/10.1021/acsnano.8b06381.

(41) Kim, H.-S.; Cook, J. B.; Tolbert, S. H.; Dunn, B. The Development of Pseudocapacitive Properties in Nanosized-MoO2. *J. Electrochem. Soc.* **2015**, *162* (5), A5083. https://doi.org/10.1149/2.0141505jes.

(42) Nakao, S.; Kamisaka, H.; Hirose, Y.; Hasegawa, T. Structural, Electrical, and Optical Properties of Polycrystalline NbO2 Thin Films Grown on Glass Substrates by Solid Phase Crystallization. *Phys. Status Solidi A* **2017**, *214* (3), 1600604. https://doi.org/10.1002/pssa.201600604.

(43) Deng, C.; Lun Lau, M.; Ma, C.; Skinner, P.; Liu, Y.; Xu, W.; Zhou, H.; Zhang, X.; Wu, D.; Yin, Y.; Ren, Y.; Perez, J.; Jaramillo, D.; Barnes, P.; Hou, D.; Dahl, M.; Williford, B.; Zheng, C.; Hui (Claire) Xiong. A Mechanistic Study of Mesoporous TiO 2 Nanoparticle Negative Electrode Materials with Varying Crystallinity for

Lithium Ion Batteries. *J. Mater. Chem. A* **2020**, *8* (6), 3333–3343. https://doi.org/10.1039/C9TA12499C.

(44) Wagemaker, M.; Mulder, F. M. Properties and Promises of Nanosized Insertion Materials for Li-Ion Batteries. *Acc. Chem. Res.* **2013**, *46* (5), 1206–1215. https://doi.org/10.1021/ar2001793.

(45) Van der Ven, A.; Bhattacharya, J.; Belak, A. A. Understanding Li Diffusion in Li-Intercalation Compounds. *Acc. Chem. Res.* **2013**, *46* (5), 1216–1225. https://doi.org/10.1021/ar200329r.

(46) Sun, G.; Sui, T.; Song, B.; Zheng, H.; Lu, L.; Korsunsky, A. M. On the Fragmentation of Active Material Secondary Particles in Lithium Ion Battery Cathodes Induced by Charge Cycling. *Extreme Mech. Lett.* **2016**, *9*, 449–458. https://doi.org/10.1016/j.eml.2016.03.018.

(47) O'Connor, D. T.; Welland, M. J.; Liu, W. K.; Voorhees, P. W. Phase Transformation and Fracture in Single LixFePO4 Cathode Particles: A Phase-Field Approach to Li–Ion Intercalation and Fracture. *Model. Simul. Mater. Sci. Eng.* **2016**, *24* (3), 035020. https://doi.org/10.1088/0965-0393/24/3/035020.

(48) Yang, Y.; Xu, R.; Zhang, K.; Lee, S.-J.; Mu, L.; Liu, P.; Waters, C. K.; Spence, S.; Xu, Z.; Wei, C.; Kautz, D. J.; Yuan, Q.; Dong, Y.; Yu, Y.-S.; Xiao, X.; Lee, H.-K.; Pianetta, P.; Cloetens, P.; Lee, J.-S.; Zhao, K.; Lin, F.; Liu, Y. Quantification of Heterogeneous Degradation in Li-Ion Batteries. *Adv. Energy Mater.* **2019**, *9* (25), 1900674. https://doi.org/10.1002/aenm.201900674.

(49) Li, J.; Zhang, Q.; Xiao, X.; Cheng, Y.-T.; Liang, C.; Dudney, N. J. Unravelling the Impact of Reaction Paths on Mechanical Degradation of Intercalation Cathodes for Lithium-Ion Batteries. *J. Am. Chem. Soc.* **2015**, *137* (43), 13732–13735. https://doi.org/10.1021/jacs.5b06178.